Coastal ocean optical influences on solar transmission and radiant heating rate

Grace C. Chang and Tommy D. Dickey

Ocean Physics Laboratory, University of California, Santa Barbara, Goleta, California, USA

[1] An extensive set of physical and optical measurements is utilized to characterize the processes and quantify parameters that contribute to the variability of solar transmission, sea surface albedo, and radiant heating rate (RHR). This study is among the first to utilize multidisciplinary observations coupled with radiative transfer simulations to investigate the impact of optical properties on solar transmission, albedo, and heating in nearshore coastal waters. The data were collected from a shallow-water coastal mooring as part of the Hyperspectral Coastal Ocean Dynamics Experiment (HyCODE) in summer 2001. Over the 41-day time series, the average loss in solar radiation was 274 W m^{-2} for mean surface radiation of 365 W m^{-2} (average solar transmission of 21%). Quantitative coherence and principle component analyses suggest that cloud cover, chlorophyll concentration (Chl), and colored dissolved organic matter (CDOM) have the greatest impacts on solar transmission variability on timescales of ~1 week. Radiative transfer simulations show that Chl, absorption, and attenuation have the most significant impact on solar transmission, whereas solar angle and cloud cover greatly influence albedo. *INDEX TERMS:* 4552 Oceanography: Physical: Ocean optics; 4572 Oceanography: Physical: Upper ocean processes; 4219 Oceanography: General: Continental shelf processes; 4504 Oceanography: Physical: Air/sea interactions (0312); *KEYWORDS:* solar transmission, ocean optics, radiant heating rate, coastal oceanography, New York Bight

1. Introduction

[2] Understanding of the transmission of solar energy through the upper ocean is essential for quantification and modeling of primary productivity and upper ocean thermo-dynamics. The focus of the present study is the relationships of bio-optical properties and light transmission with thermodynamics of the upper ocean: sea surface albedo, solar transmission, and radiant heating rate (RHR). The temporal and spatial variability of spectral solar transmission is dependent on the in-water spectral solar diffuse attenuation coefficient and the sea surface albedo (defined below). In turn, the variability of the spectral solar attenuation coefficient and albedo are influenced by meteorological and upper ocean physical processes and bio-optical properties. Solar transmission and ocean radiant heating affect the intensity and depth of upper water column stratification on timescales from a day to seasons [e.g., *Klein*, 1980; *Dickey and Simpson*, 1983; *Woods et al.*, 1984; *Dickey et al.*, 1998; *Dickey and Falkowski*, 2002]. Strongly stratified waters can impact upper ocean ecology by limiting the movement of nutrients and particles, including phytoplankton, from the lower to upper water column and vice versa. This situation can inhibit nutrient entrainment and availability and possibly vertical migration, especially in upwelling regions. A

stable and shallow thermocline may also lead to photo-bleaching of phytoplankton and photo-oxidation of colored dissolved organic matter (CDOM) by trapping primary producers and CDOM in surface waters of high intensity solar radiation. Water quality in coastal areas can also be affected by the intensity and depth of upper water column stratification. Riverine or sewage inputs, pollutants, and suspended matter can be trapped in the upper water column.

[3] Variability of solar transmission, albedo, and RHR has been addressed for open ocean environments. However, few studies have focused on coastal waters (see review by *Dickey and Falkowski* [2002]), where optical and physical processes have been found to be more complex than in the open ocean. Optical properties and physical processes in coastal waters are more variable on short time and space scales [*Chang and Dickey*, 2001; *Chang et al.*, 2002] as compared to the open ocean because: 1) freshwater inputs often influence the fluid stratification and dynamics, 2) pollutants and other runoff materials are often trapped near the ocean surface, 3) there are generally more sources of particulate matter from rivers and storm water runoff and sediment resuspension events [e.g., *Nittrouer and Wright*, 1994], 4) CDOM concentrations are higher and more variable [*Boss et al.*, 2001], and 5) biological productivity and diversity are much greater, thus associated optical and physiological characteristics are more variable [e.g., *Sosik et al.*, 2001].

[4] Past open ocean studies of solar transmission and ocean radiant heating have most often employed numerical models to simulate the upper ocean with respect to meteorological and physical processes. These numerical models have been coupled with empirical relationships to compute the diffuse attenuation coefficient of light based on optical water types or measured variables such as chlorophyll fluorescence or chlorophyll concentration [e.g., *Simpson and Dickey*, 1981; *Dickey and Simpson*, 1983; *Zaneveld et al.*, 1981; *Lewis et al.*, 1983; *Katsaros et al.*, 1985; *Kirk*, 1988; *Lewis et al.*, 1990; *Morel and Antoine*, 1994; *Siegel et al.*, 1995; *Dickey et al.*, 1998; *Ohlmann et al.*, 2000; *Ohlmann and Siegel*, 2000]. In a recent study, *Ohlmann et al.* [2000] utilized irradiance measurements from the equatorial Pacific and a radiative transfer model to investigate optical influences on open ocean radiant heating. Their simulations indicated that cloud cover, solar zenith angle, and chlorophyll concentration had the greatest effects on solar transmission and heating at their open ocean site. More recently, the Surface Heat Budget of the Arctic (SHEBA) experiment provided new insights into the effects of optical properties on heating of Arctic waters. In particular, *Pegau* [2002] found that absorption by CDOM can increase heating by ~30% in the visible wavelengths ($\lambda = 350-700$ nm) in the top 10 m of the Arctic Ocean, resulting in higher melting rates of ice.

[5] Observational studies of the influences of nearshore coastal ocean processes on solar transmission and ocean radiant heating rates are rare. One example is the Coastal Transition Program, where *Ramp et al.* [1991] showed near surface (upper 2 m) temperatures to be significantly enhanced (by up to 4.7°C) within a turbid patch of water off Point Arena, California. Another relevant example includes a study in the Gulf of Maine where coccolithophore blooms were found to be responsible for increasing near surface temperatures by about 0.32 °C day^{-1} compared with values of 0.06 °C day^{-1} outside the bloom region [*Ackleson et al.*, 1988, 1994; *Balch et al.*, 1991]. Satellite-derived surface temperature data showed warmer water (by ~5 °C) within the bloom area as compared with adjacent outside waters. At high concentrations, coccolithophores are highly reflective (because of external calcium carbonate plates, or coccoliths), often causing multiple scattering and increases of light absorption near the surface. This allows less light to penetrate to depth, effectively trapping heat near the surface.

[6] Our primary objective is to couple extensive coastal ocean optical and physical data with radiative transfer simulations to evaluate the effects of bio-optical properties on solar transmission, sea surface albedo, and upper ocean RHR. We utilize a set of interdisciplinary time series measurements collected during the ONR-sponsored Hyperspectral Coastal Ocean Dynamics Experiment (HyCODE) off the coast of New Jersey in 24 m water depth (Figure 1). This study is among the first to utilize multidisciplinary observations coupled with radiative transfer simulations to investigate the impact of optical properties on thermodynamics in nearshore coastal waters.

[7] The solar transmission function, Tr(z), is defined (following *Ohlmann et al.* [2000]) as the ratio of spectrally integrated net irradiance measured at a depth, z (m), to spectrally integrated downwelling irradiance measured just above the sea surface:

$$Tr(z) = E_n(z)/E_d(0^+), \tag{1}$$

where

$$E_n(z) = E_d(z) - E_u(z) \tag{2}$$

and $E_d(z)$ and $E_u(z)$ are spectrally integrated downwelling and upwelling irradiances at a depth, z, both in units of W m^{-2} (W m^{-2} nm^{-1} for spectral irradiance). The solar transmission function can also be presented spectrally as Tr(z, λ) or

$$Tr(z, \lambda) = E_n(z, \lambda)/E_d(0^+, \lambda) \tag{3}$$

and

$$E_n(z, \lambda) = E_d(z, \lambda) - E_u(z, \lambda). \tag{4}$$

We calculated Tr(z, λ) using measured irradiances at wavelengths between 400 and 800 nm (see Methods). The definition of Tr(z) includes effects of the air-sea interface, or the component of radiation leaving the surface of the ocean. This component of radiation can be written as (following *Ohlmann et al.* [2000]):

$$\alpha_a = 1 - [E_n(0^-)/E_d(0^+)] \tag{5a}$$

or

$$\alpha_a = 1 - Tr(0^-) \tag{5b}$$

where Tr(0$^-$) is the spectrally integrated transmission just below the sea surface, or

$$Tr(0^-) = E_n(0^-)/E_d(0^+) \tag{6}$$

where

$$E_n(0^-) = E_d(0^-) - E_u(0^-). \tag{7}$$

Similar to the solar transmission function, the component of radiation leaving the sea surface can be expressed spectrally:

$$\alpha_a(\lambda) = 1 - Tr(0^-, \lambda). \tag{8}$$

Sea surface albedo (α) is often defined as the combination of water-leaving radiation (α_a) and the Fresnel reflection (α_b) off the sea surface. We estimated sea surface albedo using computed water-leaving radiation (equations (5)–(8); $\lambda = 400-800$ nm) added to modeled Fresnel reflection (see details regarding Hydrolight 4.1 below; *Mobley*, 1994). We express Tr(z), Tr(z, λ), and α, and $\alpha(\lambda)$ as percentages throughout this paper (equations (1), (3), (5), and (8) multiplied by 100). The radiant heating rate, RHR(z) (°C s^{-1}), is defined as the average rate that solar radiation heats the upper ocean of layer thickness, z (also following *Ohlmann et al.* [2000]):

$$RHR(z) = [E_n(0^-) - E_n(z)]/[\rho(z)\, c_p z] \tag{9}$$

where $\rho(z)$ is the density of seawater (kg m^{-3}) at depth, z, and c_p is the specific heat of seawater (~4100 J kg^{-1} °C^{-1}).
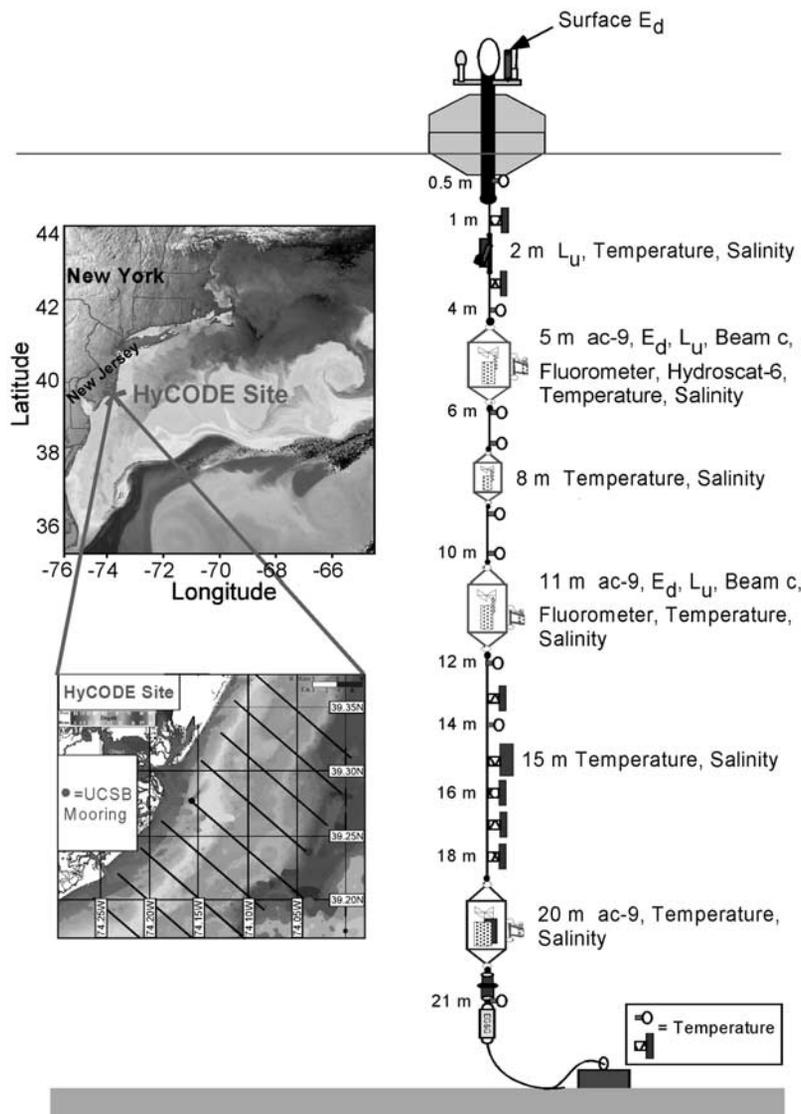
Figure 1. Map of the HyCODE site and a schematic diagram of the HyCODE mooring.

In the equations above, we specify depth, z, to be the mixed layer depth (MLD; z_{ML} = MLD). For comparison purposes, we also computed Tr(z) and RHR(z) for z = 5 m. Note: solar transmission for visible wave bands (λ = 400 – 800) has different effects on radiant heating rate as compared to transmission for the near-infrared wave bands, which are completely absorbed within the top half-meter of the water column. Therefore, we calculated RHR(z) for the visible wavelengths (λ = 400 – 800 nm; irradiances were only measured for λ = 400 – 800 nm). To account for total radiant heating (RHR(z) at λ = 400 – 2500 nm), we assumed that $E_{vis}:E_{tot}$ = 0.43, where E_{vis} is irradiance at the visible wavelengths and E_{tot} is total irradiance [*Baker and Frouin*, 1987].

2. Methods

2.1. Observational Data

[8] Instruments were deployed on a mooring during HyCODE between June 19 and August 6, 2001. These instruments concurrently collected high temporal resolu-

tion physical and optical measurements at several depths off of the coast of New Jersey (about 39°20′N, 74°05′W) in 24 m water depth ($\sim$25 km offshore; Figure 1). Physical and optical instruments included: hyperspectral radiance (at 2, 5, and 11 m depths) and irradiance (just above the surface, and at 5 and 11 m depths) sensors (Satlantic, Inc. MiniSpecs; 3.3 nm resolution for visible wavelengths, λ = 350 – 800 nm); spectral absorption-attenuation meters (WET Labs, Inc. ac-9s; λ = 412, 440, 488, 510, 532, 555, 650, 676, and 715 nm; *Moore et al.*, 1992) at 5, 11, and 20 m; beam transmissometers (λ = 660 nm; WET Labs, Inc. C-Stars) and fluorometers (WET Labs, Inc. WETStars) at 5 and 11 m; a backscattering instrument (λ = 442, 470, 510, 589, 620, and 671 nm; HOBI Labs HydroScat-6; *Maffione and Dana*, 1997) at 5 m; temperature sensors at about every 1 m from near-surface to near-bottom; and salinity sensors at 2, 5, 8, 11, 15, and 20 m (Figure 1). For more details regarding mooring instrumentation and a description of physical processes and optical properties at the HyCODE site, see *Jiang et al.* [2001] and *Chang et al.* [2002].

Table 1. Mean, Minimum, and Maximum Values of Various Parameters for the Daily Noontime 41-Day and 1 July 2001 13-Hour Time Series

	Wind Speed, m s^{-1}	CI,[a] %	MLD,[b] m	Tr(z$_{ML}$),[c] %	α,[d] %	RHR,[e] Deg C hr^{-1}	Chl,[f] μg l^{-1}	a(412),[g] m^{-1}	c(650),[h] m^{-1}
				41-Day Time Series (20 June to 30 July 2001)					
Mean	5.1	21.2	6.05	21.3	3.9	0.14	3.09	0.65	1.56
Min[i]	2.3	0	1.0	0.4	3.4	0.02	1.02	0.44	0.55
Max[j]	9.9	87.4	15	68.2	5.3	0.35	5.89	1.06	2.47
				13-Hour Time Series (0600 to 1800 LT) on 1 July 2001					
Mean	6.0	0.7	8.2	5.0	7.3	0.06	2.90	0.48	0.77
Min	3.0	0	8	3.9	3.6	0	2.27	0.44	0.53
Max	8.6	5.6	9	7.4	18.6	0.11	3.85	0.52	0.92

[a]CI, cloud index.
[b]MLD, mixed layer depth.
[c]Tr(z$_{ML}$), integrated solar transmission function at the MLD (λ = 400 – 800 nm).
[d]α, integrated sea surface albedo (λ = 400 – 800 nm).
[e]RHR, radiant heating rate (λ = 400 – 2500 nm; at the MLD).
[f]Chl, chlorophyll concentration.
[g]a(412) = absorption coefficient (total minus water) at 412 nm.
[h]c(650), attenuation coefficient (total minus water) at 650 nm.
[i]Min, minimum.
[j]Max, Maximum.

[9] Complementary HyCODE data included volume scattering functions (VSFs) and meteorological data. The spectral VSF is defined as the differential scattering cross section per unit volume. Integration of the VSF over all solid angles gives the total scattering coefficient. VSFs at 532 nm were measured several times at our mooring location on July 25, 2001 with a prototype VSF meter [*Chang et al.*, 2003; *Lee and Lewis*, 2003]. VSF measurements were taken at various discrete depths within the mixed layer (generally <5 m water depth) over a range of scattering angles (0.5° to 177.6°, 0.6° resolution). A meteorological tower located onshore, approximately 25 km from our mooring, measured hourly wind speed and direction, air temperature, barometric pressure, and relative humidity. Our computations (see below) involved daily noontime values of all relevant parameters over a 41-day time series (June 20–July 30, 2001) in addition to hourly averaged values between 0600 and 1800 LT on the "sunniest" day of our time series (July 1, 2001; E$_{max}$; see below for definition) to assess the effects of solar angle.

2.2. Hydrolight Modeling

[10] The well-documented Hydrolight model solves radiative transfer equations in water based on invariant imbedding theory [*Mobley*, 1994]. Hydrolight output data relevant to this study include Fresnel reflectance for sea surface albedo estimations, upwelling and downwelling irradiance, and the diffuse attenuation coefficients for upwelling radiance and downwelling irradiance for closure purposes. Necessary inputs to Hydrolight include the boundary conditions and the inherent optical properties (IOPs). Hydrolight input boundary conditions include wind speed, solar angle, cloud cover, downwelling sky irradiance, and ocean bottom type. Measured wind speed and downwelling sky irradiance (measured by the hyperspectral irradiance sensor mounted just above the sea surface) were provided for the model. The solar zenith angle was computed using equations (2-2) and (2-3) of *Kirk* [1994]. These computations require latitude, Julian day, and the sampling time of day. Cloud cover index, CI (Table 1), was computed using the following relationship (expressed as a percentage):

$$CI = 100*[1 - (E/E_{max})], \qquad (10)$$

where E is measured daily noontime irradiance and E$_{max}$ is the maximum value of measured daily noontime irradiance throughout the 41-day time series, measured by the irradiance sensor mounted just above the sea surface (not equivalent to clear sky irradiance due to aerosol scattering and absorption off coastal New Jersey). Therefore, CI = 0 represents a cloud-free sky and CI = 100% a completely overcast sky. We also assumed optically deep waters, i.e., the ocean bottom reflectance is justifiably neglected.

[11] Inherent optical properties (IOPs) are optical properties of the water column that are dependent only on the aquatic medium itself, not on the geometric structure of the light field [*Kirk*, 1994; *Mobley*, 1994]. We assumed a two-component water body with pure water [*Pope and Fry*, 1997] as component 1 and particulate plus dissolved matter as component 2. The input IOPs were measured during the HyCODE experiment, thus we were able to provide profiles of total spectral absorption minus the contribution from water, $a_{t-w}(\lambda)$, total spectral attenuation minus water, $c_{t-w}(\lambda)$, and total spectral scattering minus water by difference, $b_{t-w}(\lambda) = c_{t-w}(\lambda) - a_{t-w}(\lambda)$, and VSF (scattering phase functions) observations. *Mobley et al.* [2002] explains the importance of the use of in situ VSF measurements as opposed to standard data sets [e.g., *Petzold*, 1972] in radiative transfer models. A phytoplankton specific absorption spectrum based on *Prieur and Sathyendranath* [1981] was assumed in order to determine how much light was absorbed by chlorophyll so that measured chlorophyll fluorescence could be included in the Hydrolight simulations.

3. Data Analyses

[12] Three separate analyses were utilized for our time series observations and the radiative transfer model, Hydro-

light 4.1 [*Mobley*, 1994]. Analysis (1) involved time series statistical analyses to determine sources of variability within our time series and dominant processes and properties that have the greatest influence on solar transmission variability throughout our 41-day time series. For Analysis (2), the effects of cloud index, solar angle, chlorophyll concentration (Chl), absorption coefficient, and attenuation coefficient on solar transmission, sea surface albedo, and RHR were investigated using observational data and Hydrolight simulations. Analysis (3) utilized Hydrolight simulations to study the influence of Chl on daily upper ocean heating rates and the time rate of change of heat content within the mixed layer.

3.1. Computation of Solar Transmission, Sea Surface Albedo, Radiant Heating Rate, and the Heat Budget

[13] Equations (1), (2), (3), and (4) were used to calculate $Tr(z_{ML})$ and $Tr(z_{ML}, \lambda)$, where depth, z_{ML}, is defined as the mixed layer depth (z_{ML} = MLD). MLD was computed using our high vertical resolution temperature measurements and a $0.25°C$ temperature criterion (Table 1; Figure 2a). MLD was also computed using $0.5°$, $1°$, and $2°C$ temperature criteria for comparison. The MLDs are quite similar (not shown); we utilize the $0.25°C$ temperature criterion for all of our computations. Spectrally integrated and spectral ($\lambda = 400$–800 nm) daily noontime values of $E_d(0^+)$, $E_d(z)$, $E_d(0^+, \lambda)$, and $E_d(z, \lambda)$ were determined using our hyperspectral radiometric measurements (at $z = 0^+$, 5, and 11 m) and the approximation of a logarithmic profile of irradiance with depth throughout the mixed layer (Figure 2b). We calculated the spectral diffuse attenuation coefficient for downwelling irradiance, $K_d(\lambda)$:

$$K_d(\lambda) = (-d/dz) \ln[E_d(z, \lambda)], \qquad (11a)$$

$$= -(1/\Delta z) \ln[E_d(z_2, \lambda)/E_d(z_1, \lambda)], \qquad (11b)$$

where z_2 and z_1 are depths 1 m apart ($\Delta z = 1$ m) and $z_2 > z_1$. $E_d(z, \lambda)$ was then computed using

$$E_d(z_1, \lambda) = E_d(z_2, \lambda)/\exp[-K_d(\lambda)\Delta z]. \qquad (12)$$

[14] We integrated between the visible wavelengths, $\lambda = 400 - 800$ nm, to obtain $E_d(0^-)$ and $E_d(z)$. In this case, we neglect the infrared wavelengths that are assumed to be completely absorbed by the water itself within the top half-meter of the water column. The infrared wavelengths are included in computations of heating (see Definitions). Measured $E_d(0^+, \lambda)$ was provided by our above-water hyperspectral irradiance sensor. $E_u(z)$ and $E_u(z, \lambda)$ were calculated using spectrally integrated and spectral radiometric measurements and Hydrolight output, and the following equations

$$E_u(z) = E_d(z)*[E_{uHL}(z)/E_{dHL}(z)], \qquad (13a)$$

$$E_u(z, \lambda) = E_d(z, \lambda)*[E_{uHL}(z, \lambda)/E_{dHL}(z, \lambda)], \qquad (13b)$$

where the subscript HL defines quantities that are determined from Hydrolight simulations. Measured IOPs (spectral absorption, scattering, and attenuation, VSFs, and

Chl) and boundary conditions (wind speed, solar angle, cloud index, $E_d(0^+, \lambda)$, and MLD or $z = 5$ m) at daily noon throughout the 41-day time series were used as inputs to these Hydrolight simulations.

[15] Spectrally integrated and spectral albedo were calculated (as above) using equations (5), (6), (7), and (8), computed $E_d(0^-)$ and $E_d(0^-, \lambda)$, and Hydrolight outputs of $E_{uHL}(0^-)$, $E_{dHL}(0^-)$, $E_{uHL}(0^-, \lambda)$, $E_{dHL}(0^-, \lambda)$, and Fresnel reflectance. Equation (9), the data and computations described above, and the assumption that $E_{vis}:E_{tot} = 0.43$ were used to compute RHR. Seawater density was evaluated using temperature and salinity measurements and the equations of state. See Table 1 for mean, minimum, and maximum values of daily noontime (41 days) and hourly (0600–1800 LT on 1 July 2001) wind speed, CI, MLD, $Tr(z_{ML})$, α, $RHR(z_{ML})$, Chl, absorption at 412 nm ($a_{t-w}(412)$), and attenuation at 650 nm ($c_{t-w}(650)$). We also computed 41-day time series of $Tr(z)$ and $RHR(z)$ for fixed $z = 5$ m to examine the effects of measured optical properties on solar transmission and radiant heating rate without the influence of water column depth.

[16] The net heat flux budget at the sea surface (units of W m^{-2}) was computed to investigate the significance of bio-optically mediated heating at the HyCODE site:

$$Q_{net} = Q_{sen} + Q_{lat} + Q_{lw}(net) + Q_{sw}(net) \qquad (14)$$

where Q_{sen} is the sensible heat flux, Q_{lat} is the latent heat flux, $Q_{lw}(net)$ is the net longwave radiation, and $Q_{sw}(net)$ is the net shortwave radiation. $Q_{sw}(net)$ was computed from the calculated radiant heating rate at the surface. The rest of the terms in the heat budget were computed using the formulae presented by *Doney* [1996]:

$$Q_{sen} = \rho_a c_{pa} C_H U_{10}(T_a - T_s) \qquad (15a)$$

$$Q_{lat} = \rho_a L_v C_E U_{10}(q_a - q_s) \qquad (15b)$$

$$Q_{lw}(net) = -\varepsilon_0 \sigma [T_a^4(0.39 - 0.05\,e_a^{0.5})F(CI) + 4T_a^3(T_s - T_a)] \qquad (15c)$$

$$F(CI) = 1 - 0.63\,CI \qquad (15d)$$

where ρ_a is air density (1.22 kg m^{-3}), c_{pa} is the specific heat of air at constant pressure (1003 J kg^{-1} K^{-1}), C_H and C_E are bulk transfer coefficients (9.7×10^{-4} and 1.5×10^{-3}, both unitless), U_{10} is the wind speed at 10 m above the sea surface (m s^{-1}), T_a and T_s are air and sea surface temperatures (both in K), L_v is the latent heat of vaporization (2.45×10^6 J kg^{-1}), q_a and q_s are air and sea specific humidity (both unitless), ε_0 is the emissivity of the Earth's surface (0.985, unitless), σ is the Stefan Boltzmann constant (5.7×10^{-8} W m^{-2} K^{-4}), e_a is the vapor pressure, and CI is the cloud index (see Equation 10).

3.2. Time Series Statistical Analyses

[17] Time series statistical analyses were performed to investigate sources and scales of variability within our
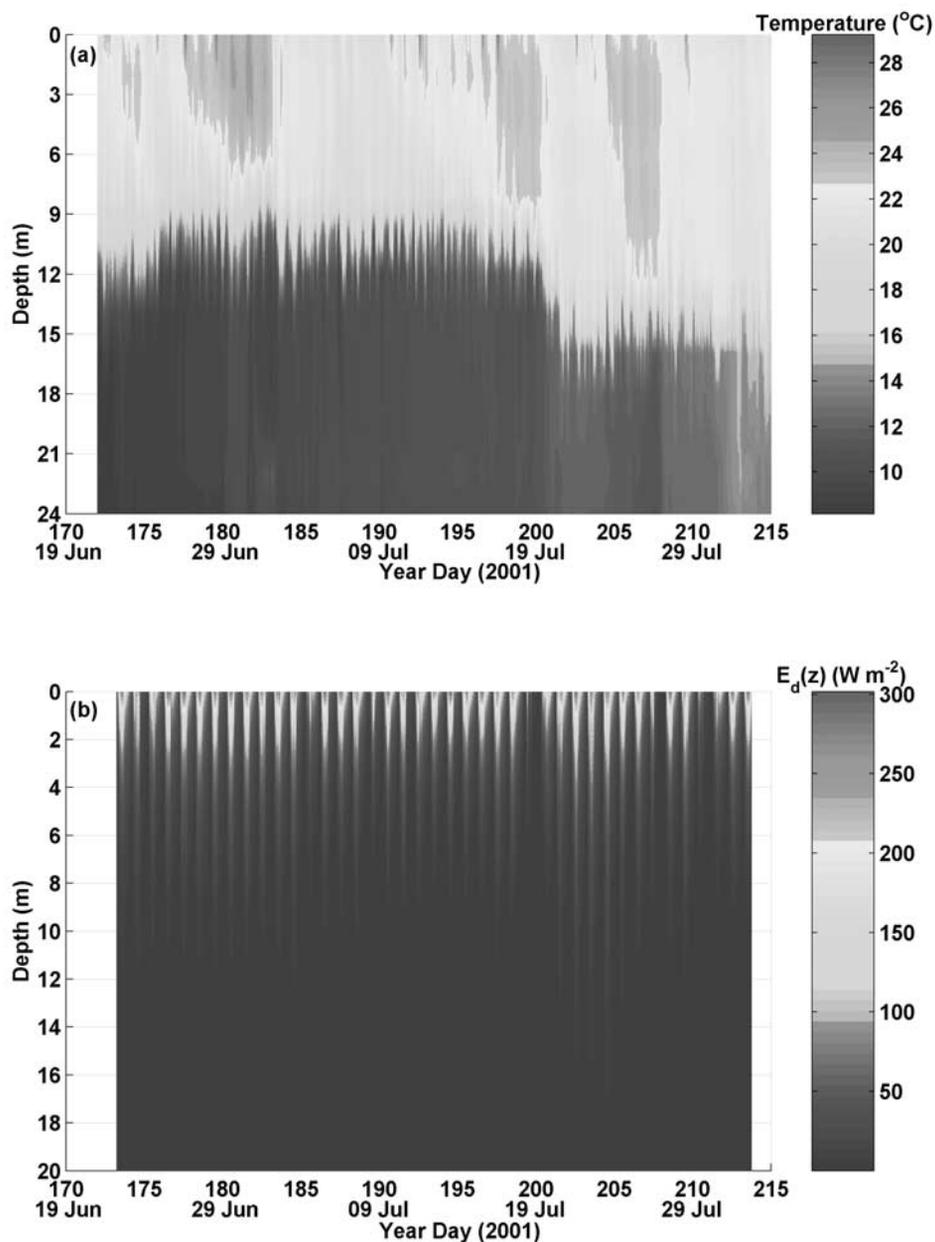
Figure 2. Time series contour plots of hourly averaged (a) temperature with depth and (b) spectrally integrated ($\lambda = 400-800$ nm) downwelling irradiance with depth, $E_d(z)$, derived from HyCODE mooring measurements and equations (11) and (12). See color version of this figure at back of this issue.

observational data set. We employed empirical orthogonal function (EOF; see *Emery and Thomson*, 1997) analysis, also known as principal component analysis, to determine the dominant modes of variability of our time series. EOF analysis compresses a data set into a series of modes (linear orthogonal functions) with associated vectors of ascending amplitudes corresponding to each mode. This method is an empirical technique used to rank the importance of a set of processes that results in variance of a data set. We performed EOF analyses for MLD, CI, chl, $a_{t-w}(412)$, $c_{t-w}(650)$, $Tr(z_{ML})$, α, and $RHR(z_{ML})$. We chose the absorption wavelength of 412 nm to investigate the influence of dissolved matter and the attenuation wavelength of 650 nm to differentiate between dissolved matter and particulates

(phytoplankton and detrital). EOF analyses were also conducted for CI, chl, $a_{t-w}(412)$, $c_{t-w}(650)$, $Tr(z)$, α, and $RHR(z)$ for $z = 5$ m to investigate the variance of the data set without the influence of a varying mixed layer. In addition, coherence and their associated phases were utilized to quantify the relationships between variables at a range of time periods. Specifically, coherence and phase estimates were made between cloud cover, solar angle, Chl at the MLD, $a_{t-w}(412)$ at the MLD, and $c_{t-w}(650)$ at the MLD with solar transmission, sea surface albedo, and RHR (i.e., coherence between cloud cover and $Tr(z_{ML})$, cloud cover and α, and cloud cover and RHR; coherence between Chl and $Tr(z_{ML})$, Chl and α, and Chl and RHR; etc.). Again, coherence and phase estimates were performed for properties at a fixed

Table 2. Hourly Values of Bio-Optical Properties Measured at 5 m Depth During Low (July 21, 2001) and High (July 12, 2001) Chlorophyll Concentration Conditions

Time of Day, LT	Chl (μg l^{-1})[a] Low/High	a(412) (m^{-1})[b] Low/High	c(650) (m^{-1})[c] Low/High
0600	1.37/4.46	0.57/0.81	0.90/2.40
0700	1.39/4.49	0.57/0.81	0.98/2.38
0800	1.47/4.47	0.57/0.82	0.93/2.36
0900	1.48/4.47	0.58/0.82	0.94/2.34
1000	1.44/4.50	0.58/0.83	0.92/2.32
1100	1.42/4.65	0.57/0.84	0.89/2.32
1200	1.38/4.72	0.57/0.84	0.86/2.33
1300	1.30/4.91	0.57/0.86	0.85/2.37
1400	1.10/5.12	0.56/0.88	0.84/2.46
1500	1.02/5.35	0.54/0.88	0.78/2.43
1600	0.95/5.58	0.55/0.90	0.80/2.71
1700	1.09/5.92	0.55/0.89	0.85/2.51
1800	1.40/5.96	0.57/0.91	0.93/2.61

[a]Chl, chlorophyll concentration.
[b]a(412), absorption coefficient (total minus water) at 412 nm.
[c]c(650), attenuation coefficient (total minus water) at 650 nm.

depth of 5 m. Statistical significance levels were calculated according to *Thompson* [1979].

3.3. Hydrolight I: Physical and Bio-Optical Effects on Solar Transmission, Sea Surface Albedo, and Radiant Heating Rate

[18] A series of five Hydrolight simulations was employed to investigate the effects of CI, solar angle, Chl, $a_{t-w}(412)$, and $c_{t-w}(650)$ on sea surface albedo, spectrally integrated (between 400 and 800 nm) and spectral solar transmission, and RHR. This sensitivity analysis is similar to that presented by *Ohlmann et al.* [2000], but we utilize directly measured coastal ocean data as inputs into Hydrolight rather than modeled bio-optical data based on open ocean parameterizations. The average measured wind speed and MLD over the 41-day time series was employed in all Hydrolight runs (5 m s^{-1} and 6 m, respectively; see Table 1 for ranges of wind speed and MLD). Therefore, all results from this analysis are independent of MLD and wind speed. When applicable, Hydrolight input profiles of spectral absorption, scattering, and attenuation and Chl were synchronized in time. For example, a noontime value of Chl = 3.0 μg l^{-1} at the MLD was found on June 21, 2001; therefore, we used spectral absorption, scattering, and attenuation data from that same day and time as input to Hydrolight. A description of the Hydrolight inputs for each of the five simulations follows:

[19] 1. Cloud index was varied from 0 to 100% in increments of 20%. The other variables were kept fixed: solar angle = 17.85° (noontime average over the 41-day time series), Chl $\approx$ 3.0 μg l^{-1} (noontime average), and absorption, scattering, and attenuation values corresponding to the Chl value, e.g., Chl $\approx$ 3.0 μg l^{-1} on June 21, 2002; therefore, we used the absorption, scattering, and attenuation spectra from June 21.

[20] 2. We varied solar angle from 0 to 80° in increments of 20°. CI was fixed at 0% and all other parameters were the same as in (1).

[21] 3. Chl was varied with values of 1.0, 1.5, 2.0, 2.5, 3.0, 3.5, 4.0, 5.0, and 6.0 μg l^{-1}. Corresponding absorption, scattering, and attenuation spectra were identified and used

as inputs. CI and solar angle were kept fixed at 0% and 17.85°, respectively.

[22] 4. We varied $a_{t-w}(412)$: $\approx$ 0.5, 0.6, 0.7, 0.8, 0.9, and 1.0 m^{-1} with corresponding scattering, attenuation, and Chl profiles used as inputs. CI and solar angle were the same as in (3).

[23] 5. The $c_{t-w}(650)$ was varied from 0.5 to 2.5 m^{-1} in increments of 0.5 m^{-1}. Corresponding absorption, scattering, and Chl profiles were identified and used as inputs. CI and solar angle were the same as in (3).

3.4. Hydrolight II: Bio-Optical Effects on Daily Radiant Heating Rate

[24] Hydrolight simulations were also used to determine the effects of Chl and optical properties on daily upper ocean radiant heating rates. Two days were chosen for this analysis: (1) "low Chl" ($\sim$1 μg l^{-1}) on July 21, 2001 and (2) "high Chl" ($\sim$5 μg l^{-1}) on July 12, 2001. Hourly spectral absorption, scattering, and attenuation and Chl profiles taken on each of the two days were utilized as inputs to the model. Table 2 shows the hourly values of Chl, $a_{t-w}(412)$ and $c_{t-w}(650)$ at 5 m, from 0600 to 1800 LT for both days. Wind speed was set at 5.0 m s^{-1}, CI set at 0%, MLD specified as 2.0 m and 6.0 m, and solar angle was computed for each day between 0600 and 1800 LT. Hydrolight output data were used to calculate the hourly RHR and the time rate of change of heat content (dH/dt; units of W m^{-2}):

$$dH/dt = \int_0^{z_{ML}} \rho(z_{ML}) c_p [dT(z_{ML})/dt] dz_{ML}, \qquad (16)$$

for low and high Chl conditions with $z_{ML} = 2.0$ and 6.0 m for comparison, where $dT(z_{ML})/dt$ is the rate of change of temperature over time (°C s^{-1}).

4. Results and Discussion

4.1. Solar Transmission, Sea Surface Albedo, and Radiant Heating Rate

[25] The 41-day time series of daily noontime values of spectrally integrated solar radiation ($\lambda = 400 - 800$ nm), CI, MLD (criterion of 0.25°C), Chl, $a_{t-w}(412)$, $c_{t-w}(650)$, Tr(z_{ML}) and Tr(5 m) ($\lambda = 400 - 800$ nm), α ($\lambda = 400 - 800$ nm), and RHR(z_{ML}) and RHR(5 m) ($\lambda = 400 - 2500$ nm) are shown in Figure 3. Spectrally integrated solar transmission function values range from 0.4 to 68% for MLDs between 1 and 15 m over the 41-day time series (Table 1 and Figures 3a and 3c). Consistent with past findings, the variability of solar transmission is most highly correlated with fluctuations in the depth of the mixed layer. This is not unexpected as transmission of light is greatly reduced as the water column deepens. Also as expected, Tr(5 m) was greater than Tr(z_{ML}) when $z_{ML} > 5$ m and *vice versa*. Qualitatively, solar transmission is also generally coherent with cloud index (Figures 3a and 3b). Sea surface albedo variability is relatively small (Figure 3h), which is similar to results by *Ohlmann et al.* [2000, Figure 5].

[26] The attenuation of solar radiation (in W m^{-2}; also referred to as solar flux difference or decrease) was defined and computed using the following equation:

$$\text{Attenuation} = \text{Incident} - \text{Incident} * \text{Tr}(z_{ML}), \qquad (17)$$
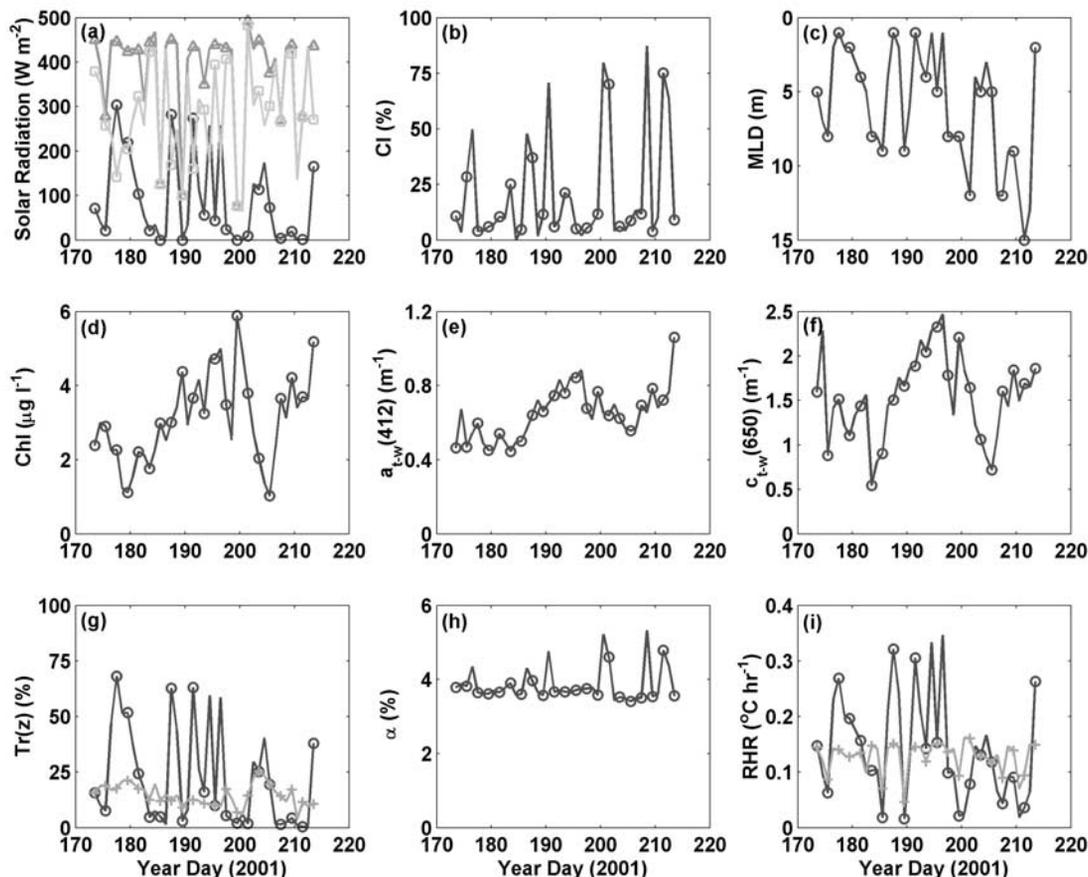
Figure 3. Forty-one-day noontime time series of (a) incident solar radiation (triangles), solar radiation at the mixed layer depth (MLD; circles), and the decrease in solar radiation (see equation (17); squares); (b) cloud index (CI); (c) MLD; measured (d) chlorophyll concentration (Chl), (e) absorption coefficient at 412 nm ($a_{t-w}(412)$), and (f) attenuation coefficient at 650 nm ($c_{t-w}(650)$); calculated (g) integrated solar transmission function at the MLD (circles) and 5 m (pluses) (Tr(z); $\lambda = 400 - 800$ nm), (h) integrated sea surface albedo (α; $\lambda = 400 - 800$ nm), and (i) radiant heating rate (RHR; $\lambda = 400 - 2500$ nm) at the MLD (circles) and 5 m (pluses), all at the HyCODE site.

where "Incident" is the surface radiation measured by the mooring radiometer located just above the sea surface and the transmission function is evaluated at the MLD ($z_{ML} = $ MLD). On average, spectrally integrated solar radiation decreased by 274 W m^{-2} (21% mean transmission); mean surface radiation was 365 W m^{-2} and mean CI was 21% (Table 1; Figure 3). The maximum loss of solar radiation (attenuation of 483 W m^{-2} for surface radiation of 492 W m^{-2}; 1.9% solar transmission) occurred during a period of 70% cloud cover, 12 m MLD, and near-average values for bio-optical properties (Year Day 201). In comparison, *Ohlmann et al.* [2000] report a $\sim$34 W m^{-2} change in net irradiance for z = 5 m in the open ocean due to varying cloud cover, solar angle, and chlorophyll concentration. *Pegau* [2002] reports a $\sim$30% increase in absorption of radiation in the upper 10 m of Arctic waters. Our coastal ocean results emphasize that the attenuation of solar energy in turbid nearshore waters is much greater than that found in clearer open ocean and Arctic waters. This can greatly affect thermodynamics and stratification of the coastal ocean.

[27] Sea surface albedo values over the 41-day time series are low; these computations were made for daily noon,

integrated between the visible wavelengths of 400 and 800 nm, i.e., high solar elevation and little reflection off of the sea surface. Sea surface albedo values exhibit a greater than fivefold change from 0600 LT (low solar elevation) to noon (high solar elevation) and from 1200 to 1800 LT (low solar elevation; Figure 4h; also see Figure 1 in *Katsaros et al.*, 1985). Figure 4 also shows hourly time series and variability of spectrally integrated solar radiation ($\lambda = 400 - 800$ nm), CI, MLD, Chl, $a_{t-w}(412)$, $c_{t-w}(650)$, Tr(z_{ML}) ($\lambda = 400 - 800$ nm), and RHR(z_{ML}) ($\lambda = 400 - 2500$ nm) from 0600 to 1800 LT (eastern daylight savings time) on July 1, 2001. Solar transmission is highest when incident solar radiation is at its peak (noon). This is consistent throughout the time series. The asymmetrical shape of the hourly time series of Tr(z_{ML}) and RHR(z_{ML}) may be attributed to the slight changes in mixed layer depth over the course of the day.

4.2. Time Series Statistical Analyses

[28] Results from EOF analyses for MLD, CI, chl, $a_{t-w}(412)$, $c_{t-w}(650)$, Tr(z_{ML}), α, and RHR(z_{ML}) indicate that 69% of the total variance of our time series is described by the first two modes. The first mode explains 37% of the
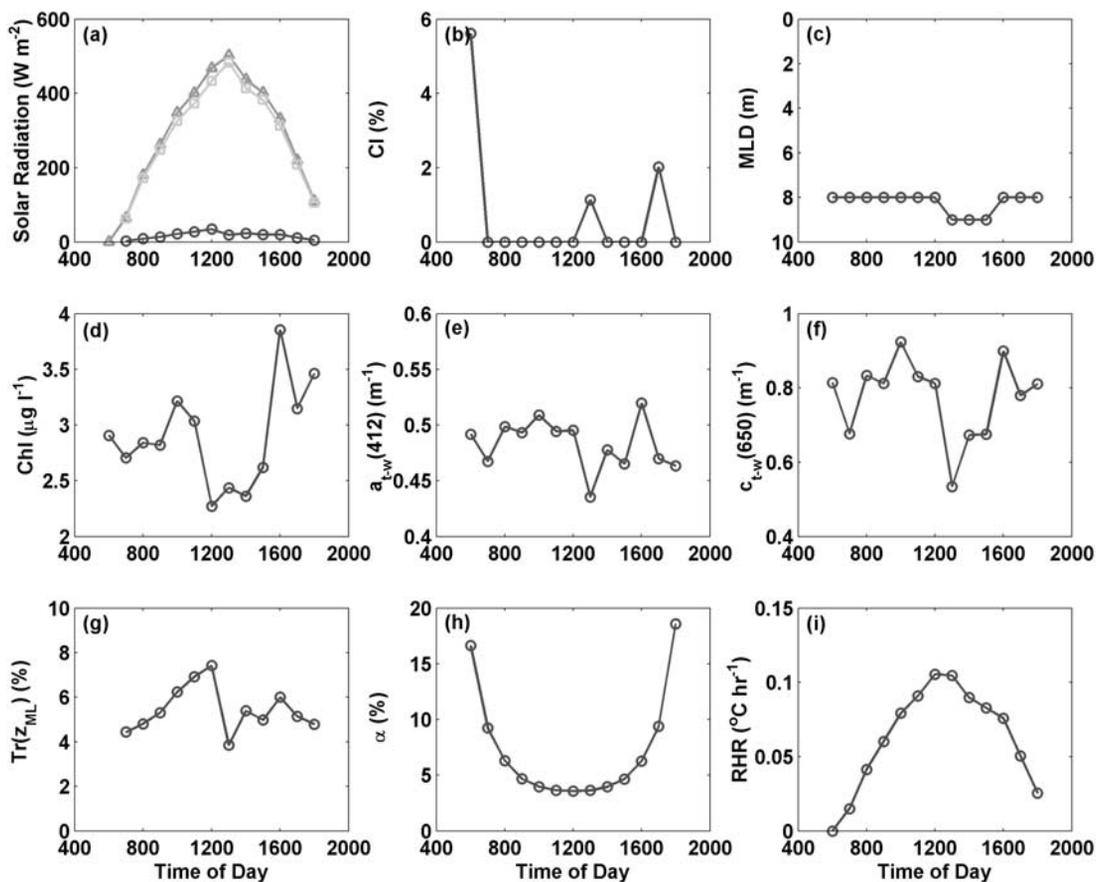
Figure 4. Hourly time series from 0600–1800 LT of (a) incident solar radiation (triangles), solar radiation at the mixed layer depth (MLD; circles), and the attenuation of solar radiation (see equation (17); squares); (b) cloud index (CI); (c) MLD; measured (d) chlorophyll concentration (Chl), (e) absorption coefficient at 412 nm ($a_{t-w}(412)$), and (f) attenuation coefficient at 650 nm ($c_{t-w}(650)$); calculated (g) integrated solar transmission function ($Tr(z_{ML})$; $\lambda = 400 - 800$ nm; $z_{ML} = $ MLD), (h) integrated sea surface albedo (α; $\lambda = 400 - 800$ nm), and (i) radiant heating rate (RHR; $\lambda = 400 - 2500$ nm; at the MLD) on July 1, 2001 at the HyCODE site.

total variance. This mode illustrates a strong inverse relationship between MLD with $Tr(z_{ML})$ and a direct correlation between MLD and $RHR(z_{ML})$. This simply indicates that MLD is the dominant influence in the variability of solar transmission and $RHR(z_{ML})$, e.g., solar transmission decreases as MLD deepens and $RHR(z_{ML})$ increases as MLD deepens. More significantly, Chl, $a_{t-w}(412)$, and $c_{t-w}(650)$ dominate the second mode (32% of the total variance); hence, the substances in the water column had a great influence on the time series variability of solar transmission, sea surface albedo, RHR, and other optical properties (not shown). Results for $z = 5$ m were slightly different than $z = $ MLD, with the first mode describing 44% of the total variance. The first mode shows a strong negative correlation between the optical properties and $Tr(5$ m$)$. This suggests that without the influence of a varying MLD, the optical properties dominated the variability of solar transmission, with Chl being the most important factor, followed by $a_{t-w}(412)$ and then $c_{t-w}(650)$.

[29] Coherence results from analysis (1) (see Methods section) indicate that MLD along with cloud cover, Chl, and $a_{t-w}(412)$ are significantly coherent with solar transmission,

sea surface albedo, and $RHR(z_{ML})$ on timescales of about one week; all with negative phase (not shown). $c_{t-w}(650)$ is not significantly coherent with transmission; therefore, CDOM most likely had a larger influence on solar transmission as compared to detrital particles. Optical results were the same for coherence analysis performed for $z = 5$ m. Past open ocean studies [*Lewis et al.*, 1983; *Siegel et al.*, 1995; *Ohlmann et al.*, 2000] have focused on phytoplankton pigments (e.g., Chl) as the only bio-optical influence on solar transmission. Our results are similar to those of *Pegau* [2002], which indicate that CDOM also has a significant impact on solar transmission. In Arctic waters, this has great implications on ice melt, sea level changes, etc. (*Pegau*, 2002). For coastal waters, absorption and attenuation derived from CDOM can contribute to the development of stratification near river outflows, thus resulting in photo-oxidation of near surface waters possibly leading to photobleaching of phytoplankton trapped in the surface mixed layer and reduced upwelling of nutrients to the upper water column, affecting upper water column ecology. River outflows can also carry agricultural and industrial runoff, which may also become trapped in the upper water column,
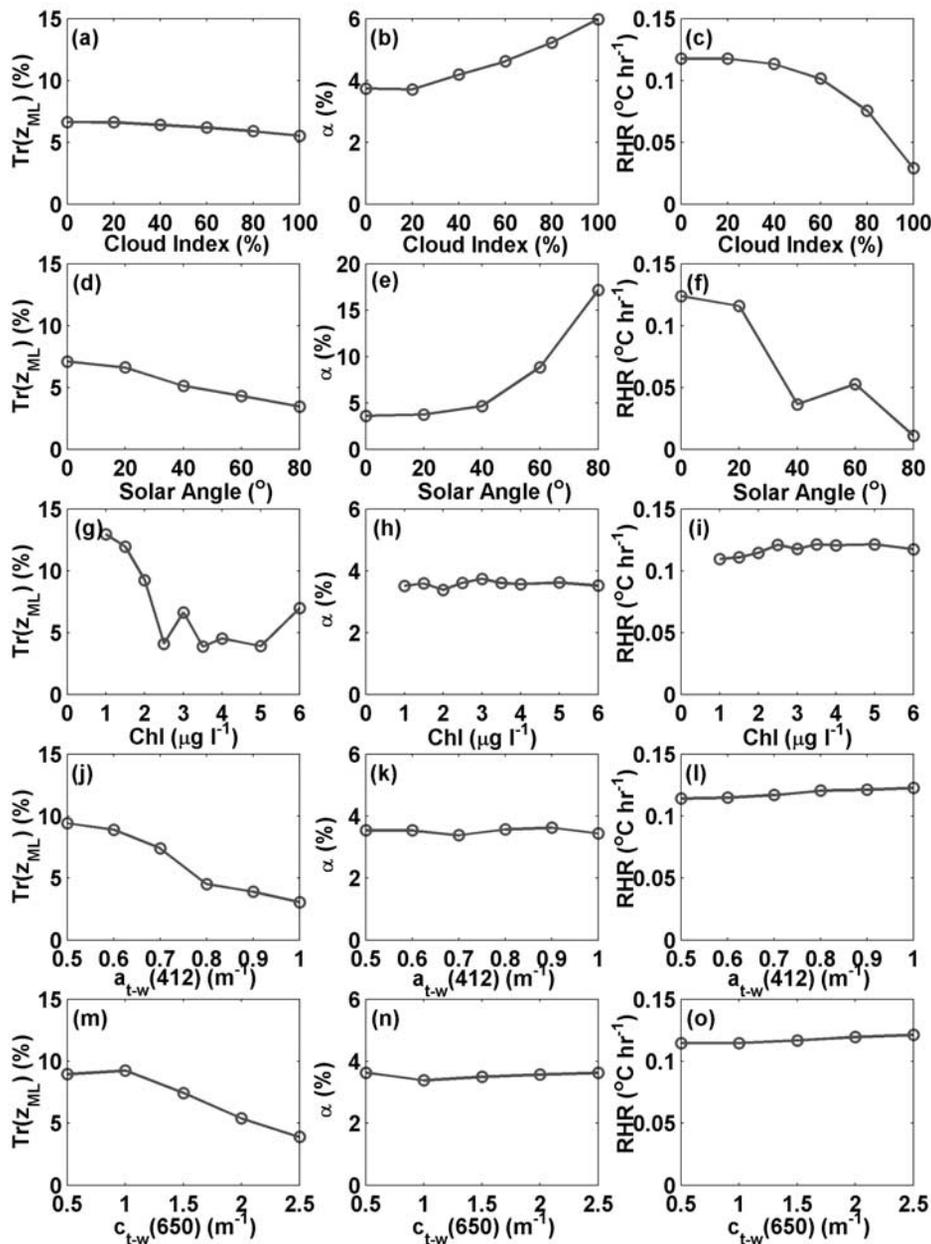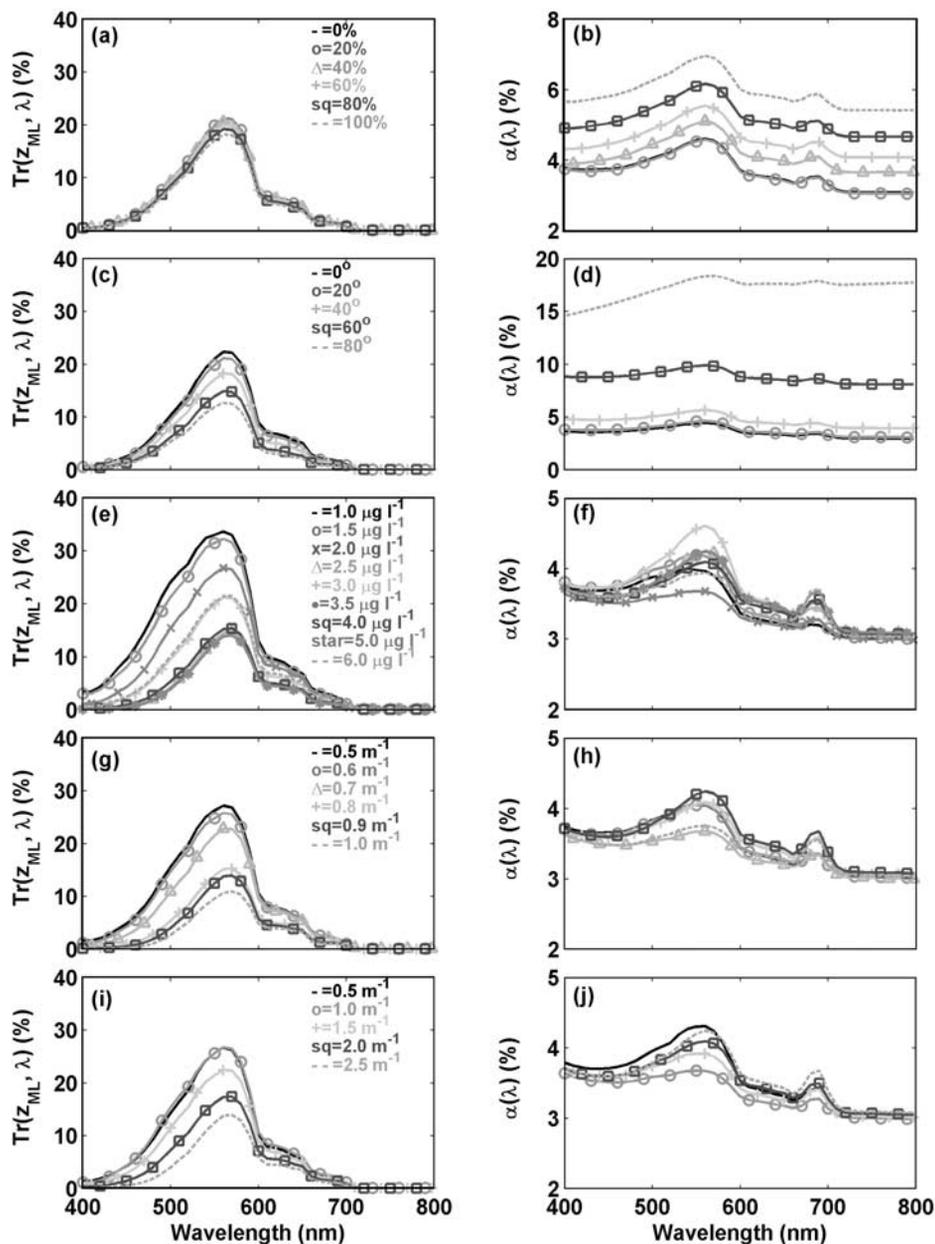
Figure 5. Spectrally integrated solar transmission function ($\mathrm{Tr}(z_{ML})$; $\lambda = 400 - 800$ nm; z_{ML} = MLD; first column), sea surface albedo (α; $\lambda = 400 - 800$ nm; second column), and radiant heating rate (RHR; $\lambda = 400 - 2500$ nm; at the MLD; third column) for varying (a), (b), and (c) cloud index (CI); (d), (e), and (f) solar angle; (g), (h), and (i) chlorophyll concentration (Chl); (j), (k), and (l) absorption coefficient at 412 nm ($a_{t-w}(412)$); and (m), (n), and (o) attenuation coefficient at 650 nm ($c_{t-w}(650)$) using Hydrolight simulations with measured bio-optical data as inputs to the model.

resulting in possible environmental problems including eutrophication.

4.3. Physical and Bio-Optical Effects on Solar Transmission, Sea Surface Albedo, and Radiant Heating Rate

[30] Spectrally integrated solar transmission, sea surface albedo, and RHR were affected differently as CI, solar angle, Chl, $a_{t-w}(412)$, and $c_{t-w}(650)$ were varied in Hydrolight simulations (Figure 5). Again, wind speed and MLD were held constant throughout these simulations in order to examine the effects of bio-optical properties on upper ocean thermodynamics without the first-order effects of the MLD. Spectrally integrated solar transmission was most affected by variations in Chl, while solar angle and cloud index were the most influential for variations in spectrally integrated sea surface albedo and RHR (Figure 5). The bumps seen in the plot of $\mathrm{Tr}(z_{ML})$ versus Chl (Figure 5g) are due to co-variations in $a_{t-w}(412)$ and $c_{t-w}(650)$ that are also used as inputs to Hydrolight.

Figure 6. Spectral solar transmission function ($Tr(z_{ML},\lambda)$; z_{ML} = MLD; first column) and sea surface albedo ($\alpha(\lambda)$; second column) for varying (a) and (b) cloud index (CI); (c) and (d) solar angle; (e) and (f) chlorophyll concentration (Chl); (g) and (h) absorption coefficient at 412 nm ($a_{t-w}(412)$); and (i) and (j) attenuation coefficient at 650 nm ($c_{t-w}(650)$) using Hydrolight simulations with measured bio-optical data as inputs to the model. Figure legends are on the $Tr(z_{ML}, \lambda)$ panels.

[31] Similar to the spectrally integrated results, variations in Chl had the greatest influence on spectral solar transmission (Figure 6), also illustrated in the variance and standard deviation of each parameter (Figures 7a and 7b). Following Chl, $a_{t-w}(412)$ and $c_{t-w}(650)$ had significant impacts on spectral solar transmission as well. Surprisingly, solar angle and CI had relatively small effects on the variability in shape and magnitude of spectral solar transmission. These results differ significantly from what has been found in past open ocean studies. In particular, *Ohlmann et al.* [2000] found that cloud index, solar angle, and Chl were the most important

factors for solar transmission variability in the equatorial Pacific.

[32] Variations in solar angle and CI had the greatest impact on spectral albedo (between 400 and 800 nm), followed by Chl, $c_{t-w}(650)$, and $a_{t-w}(412)$ (Figures 6 and 7c and 7d). This is to be expected as the solar angle of incidence has been shown to have the most influence on the intensity of reflection off of a water body.

4.4. Bio-Optical Effects on Daily Radiant Heating Rate

[33] Hydrolight simulations using measured IOPs for two days (July 21 and July 12, 2001) as inputs were
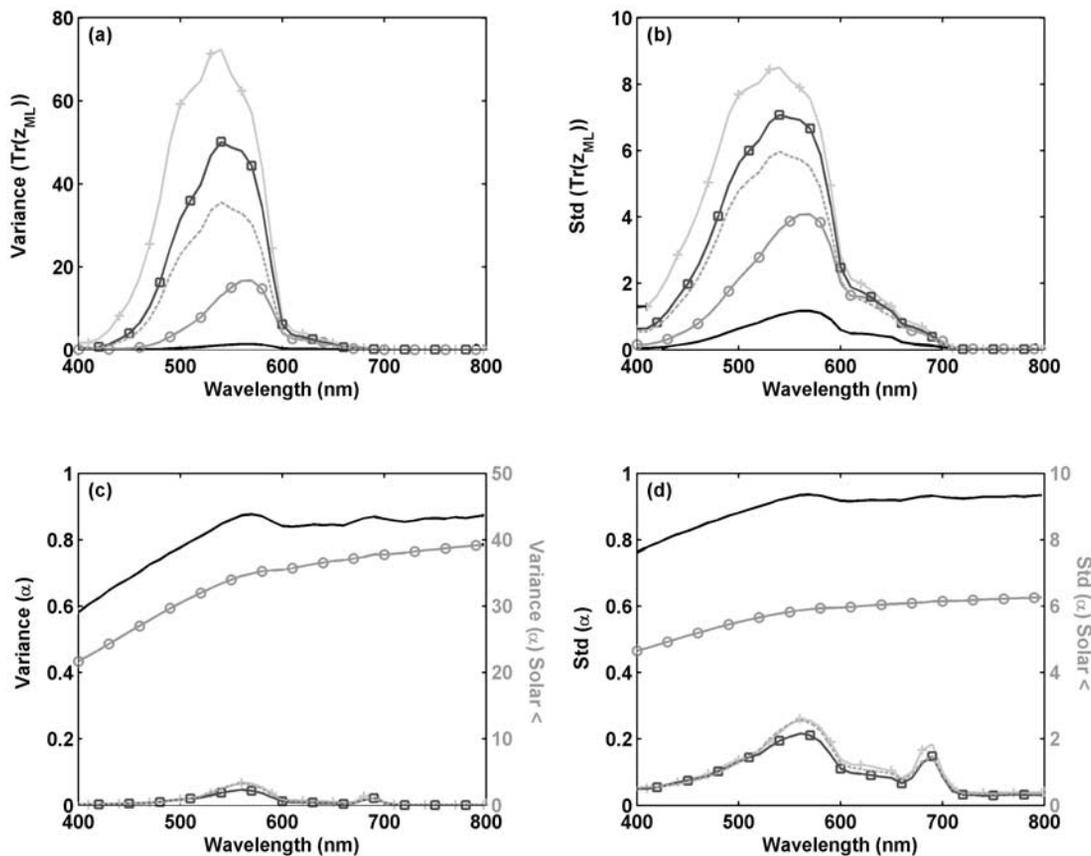
Figure 7. Variance (first column) and standard deviation (second column) of (a) and (b) spectral solar transmission function ($Tr(z_{ML}, \lambda)$; z_{ML} = MLD), and (c) and (d) sea surface albedo ($\alpha(\lambda)$) with varying cloud index (CI; solid lines), solar angle (Solar <; circles), chlorophyll concentration (Chl; pluses), absorption coefficient at 412 nm ($a_{t-w}(412)$; squares), and attenuation coefficient at 650 nm ($c_{t-w}(650)$; dashed lines).

employed to determine the effects of Chl and optical properties on daily upper ocean radiant heating rates (see Methods section for model input details). The average hourly (0600–1800 LT) difference between spectrally integrated solar transmission for low (mean Chl = 1.29 μg l^{-1}) and high (mean Chl = 4.97 μg l^{-1}) Chl conditions was 13.76% (Figure 8; Table 2; for MLD = 2 m for both Chl cases). Spectral transmission differences generally matched the shape of a phytoplankton absorption curve, with peaks at 440 and 680 nm (chlorophyll absorption peaks; Figure 8). This is to be expected since the varying Hydrolight input parameter is Chl (with co-varying absorption, scattering, and attenuation coefficients). Sea surface albedo was virtually identical for low and high Chl conditions. This result is unexpected; logically, clearer waters should exhibit higher sea surface albedo. A possible explanation is the presence of higher concentrations of particulate matter (phytoplankton and detritus), leading to higher scattering during high Chl conditions. Hourly RHR generally increased from 0600 to 1200 LT and then decreased from 1200 to 1800 LT, following the trend in solar radiation (Figure 8). The largest difference of RHR between high and low Chl occurred just after noon. On average, the difference for RHR between high and low Chl

low Chl conditions was ~0.2°C (13hr)$^{-1}$ despite the ~14% difference in solar transmission.

[34] The daily time series of RHR are similar in shape and magnitude for 2 and 6 m MLD and similar in shape to the time series of the time rate of change of heat content (dH/dt). The magnitude of dH/dt, however, is much greater for 6 m MLD as compared to 2 m MLD (Figure 9) because of the greater depth of integration. Therefore, during periods of deep mixing, dH/dt of the upper mixed layer can be orders of magnitude greater than that for low mixing conditions. This has implications on the parameterization and modeling of the heat budget (see Equations 14 and 15). The variability of net heat flux is primarily driven by changes in the net shortwave radiation; $Q_{sw}(net) \approx Q_{net}$. The sensible heat flux approximately balances the contributions of latent heat flux and longwave radiation (data not shown). Therefore, it can be inferred that fluctuations in the mixed layer bio-optical properties can greatly affect the heat budget at the HyCODE site. Unfortunately heat budget modeling efforts for HyCODE are difficult because MLDs were unpredictable at the HyCODE mooring site in summer 2001. Wind speeds were not significantly coherent with MLD; horizontal and vertical advection (primarily induced by upwelling and downwelling regimes) strongly
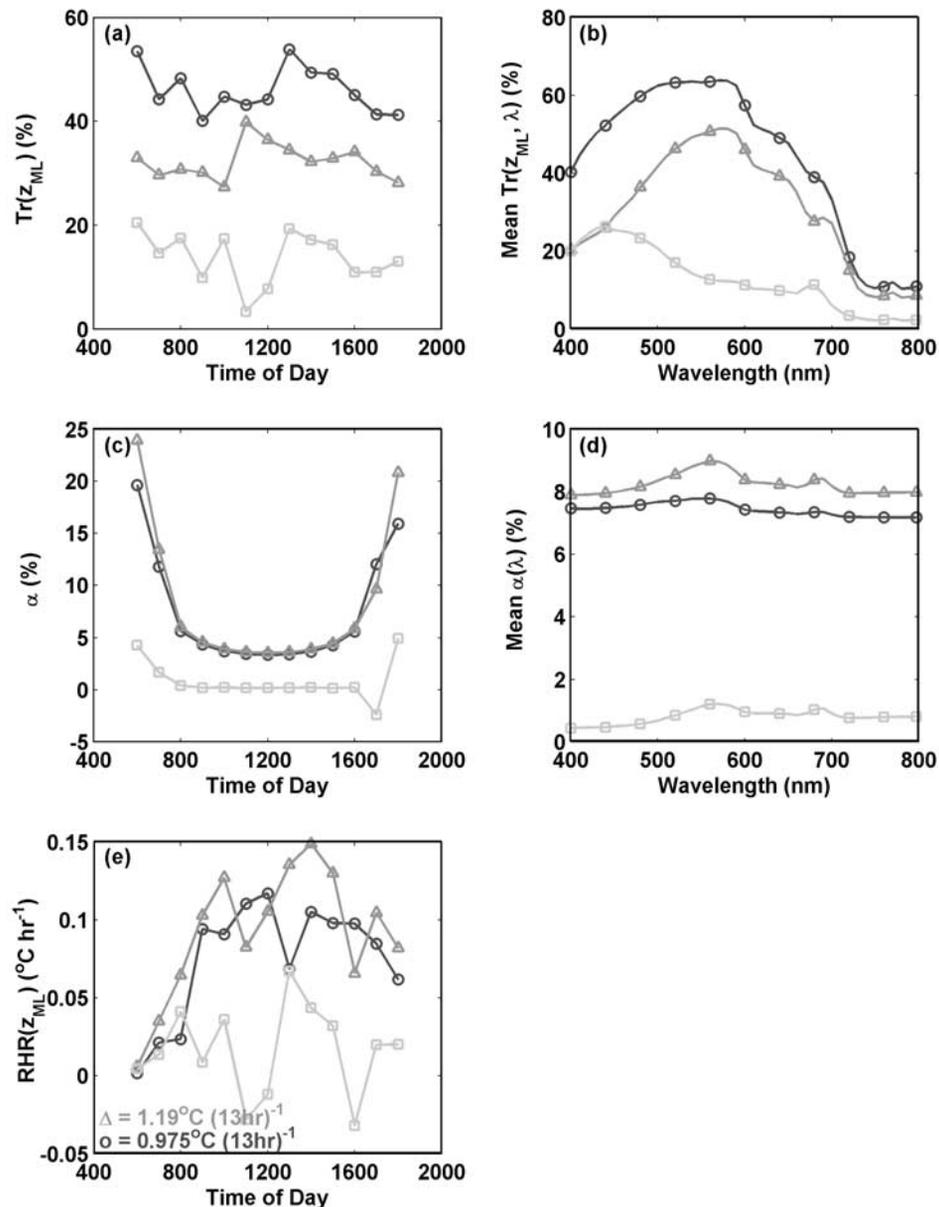
Figure 8. Hourly time series of (a) spectrally integrated solar transmission function ($Tr(z_{ML})$; $\lambda = 400 -$ 800 nm; z_{ML} = MLD), (b) mean spectral solar transmission function ($Tr(z_{ML}, \lambda)$; z_{ML} = MLD), (c) spectrally integrated sea surface albedo (α; $\lambda = 400 - 800$ nm), (d) mean spectral sea surface albedo ($\alpha(\lambda)$), and (e) radiant heating rate (RHR; $\lambda = 400 - 2500$ nm; at the MLD) for Hydrolight simulated (measured bio-optical properties used as inputs) low (July 21, 2001; circles) and high (July 12, 2001; triangles) chlorophyll concentration conditions (see Table 2) with 2 m mixed layer depth. Squares denote the difference between high and low Chl conditions. Note: daily integrated (13-hr) RHR values for high (triangles) and low (circles) Chl conditions are found in (e).

affected upper water column stratification (see *Chang et al.*, 2002).

4.5. Implications of Results

[35] Bio-optical feedbacks are important for the vertical and horizontal structure of the coastal ocean as related to upper water column thermodynamics [*Edwards et al.*, 2001]. A few different scenarios related to spatial gradients in optical absorbers and scatterers in the coastal ocean are

described here. Keep in mind that the situations depicted here are simplistic; other complicating factors (e.g., current structure and advection, salinity gradients and advection) could have effects on coastal ocean processes as well. A phytoplankton bloom with an accompanying increase in CDOM would likely result in greater trapping of heat near the surface of the ocean. This would lead to the strengthening of the thermocline and thus, retention of phytoplankton in the euphotic layer. In a location with little grazing and
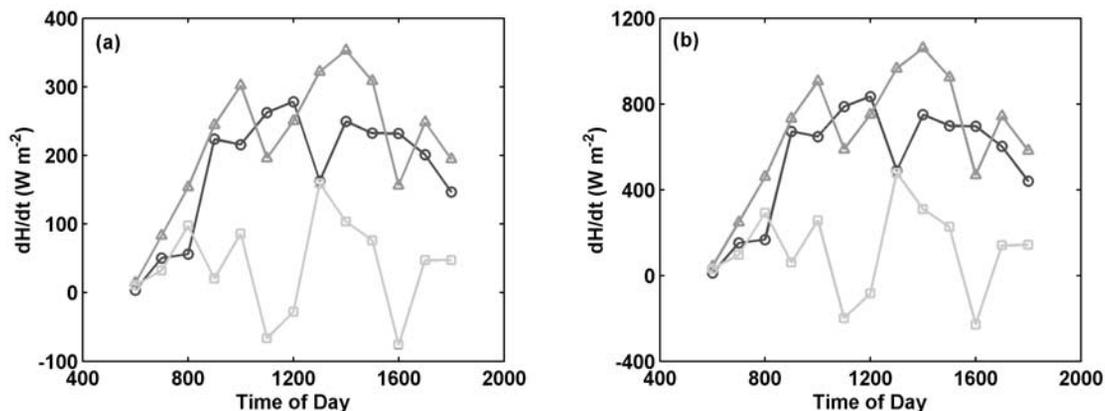
Figure 9. Hourly time series of computed time rate of change of heat content (dH/dt) for low ($\sim$1 μg l^{-1}; July 21, 2001; circles) and high ($\sim$5 μg l^{-1}; July 12, 2001; triangles) chlorophyll concentration conditions for (a) 2 m mixed layer depth and (b) 6 m mixed layer depth. Squares denote the difference between high and low Chl conditions.

a steady supply of nutrients through horizontal advection, enhanced production would continue until nutrients become limited with relation to the phytoplankton population, or phytoplankton become photo-inhibited. If excessive grazing exists or there is no horizontal supply of nutrients, the strong and stable thermocline would limit vertical transport or mixing of nutrients, resulting in the decline of the phytoplankton population in surface waters.

[36] Bio-optical feedbacks can also affect thermal frontal characteristics. A phytoplankton bloom on the "warm" side of a thermal front could potentially result in enhancement of the front, as phytoplankton would cause more heat trapping and near surface stratification. On the other hand, thermal fronts could be eroded if the phytoplankton bloom occurs on the "cool" side of the front. Enhanced warming would occur on the "cooler" side of the front, leading to reduction of the thermal gradient.

5. Summary

[37] Physical and bio-optical time series data coupled with Hydrolight simulations were used to characterize the processes and parameters that contributed to the variability of solar transmission, sea surface albedo, and upper ocean RHR in coastal waters. The data were collected from a mooring off the coast of New Jersey in 24 m water depth during HyCODE in summer 2001. Three separate analyses were employed to investigate variability and relationships between solar transmission, sea surface albedo, and RHR with substances comprising the water column: (1) time series statistical analyses; (2) analyses of processes and parameters affecting Tr(z), α, and RHR(z) using Hydrolight simulations; and (3) Hydrolight simulations to investigate bio-optical and physical effects on heating rates and the time rate of change of heat content.

[38] 1. Over the 41-day HyCODE mooring time series, spectrally integrated solar radiation (λ = 400–800 nm) at daily noon decreased by an average of 274 W m^{-2} for mean surface radiation of 365 W m^{-2}; average solar transmission was 21%. Qualitatively, solar transmission variability was highly correlated with MLD and somewhat correlated with

cloud cover. Quantitative coherence analyses indicate that cloud cover, Chl, and CDOM had the greatest influence on solar transmission at timescales of about one week (all with negative phase). EOF analyses indicate that Chl, CDOM, and other particulates in the water column had a great influence on the time series variability of solar transmission.

[39] 2. Results from Hydrolight simulations demonstrate that Chl, followed by $a_{t\text{-}w}(412)$ and $c_{t\text{-}w}(650)$, had the most significant impact on spectral and spectrally integrated (λ = 400 – 800 nm) solar transmission variability within the MLD. Solar angle and cloud cover greatly influenced spectral and spectrally integrated albedo.

[40] 3. For low ($\sim$1 μg l^{-1}) and high ($\sim$5 μg l^{-1}) Chl conditions (July 21 and 12, respectively; MLD = 2 m for both Chl cases), Hydrolight simulations reveal that the difference between RHR (λ = 400 – 2500) over the hourly time series from 0600 to 1800 LT (EDT) was $\sim$0.2°C (13hr)$^{-1}$. Spectrally integrated solar transmission (between 400 and 800 nm) was $\sim$14% lower during high Chl conditions as compared to low Chl conditions. The spectral difference between high Chl and low Chl spectral solar transmission matched the shape of a phytoplankton absorption curve, with peaks at 440 and 680 nm (chlorophyll absorption peaks). Sea surface albedo values were virtually the same for both conditions. The mean hourly time rate of change of heat content was $\sim$217 W m^{-2} for 2 m MLD and $\sim$652 W m^{-2} for 6 m MLD, both during high Chl conditions.

[41] This study is among the first to utilize physical and optical observations coupled with radiative transfer simulations to investigate the impact of bio-optical properties on solar transmission and heating of a water body. This is also one of the few studies of solar transmission and RHR performed in coastal waters. Our findings suggest that CDOM and possibly detritus can have a significant impact on the transmission of solar radiation through the upper water column in coastal waters and hence the radiant heating rate and the heat budget. This differs from past open ocean studies that have focused on phytoplankton pigments (e.g., Chl) as the only bio-optical influence on solar transmission. Our coastal ocean results also emphasize

that the attenuation of solar energy in turbid nearshore waters is much greater than that found in clearer open ocean and Arctic waters. In addition, the time rate of change of heat content of the upper mixed layer can increase by orders of magnitude during periods of deep mixing.
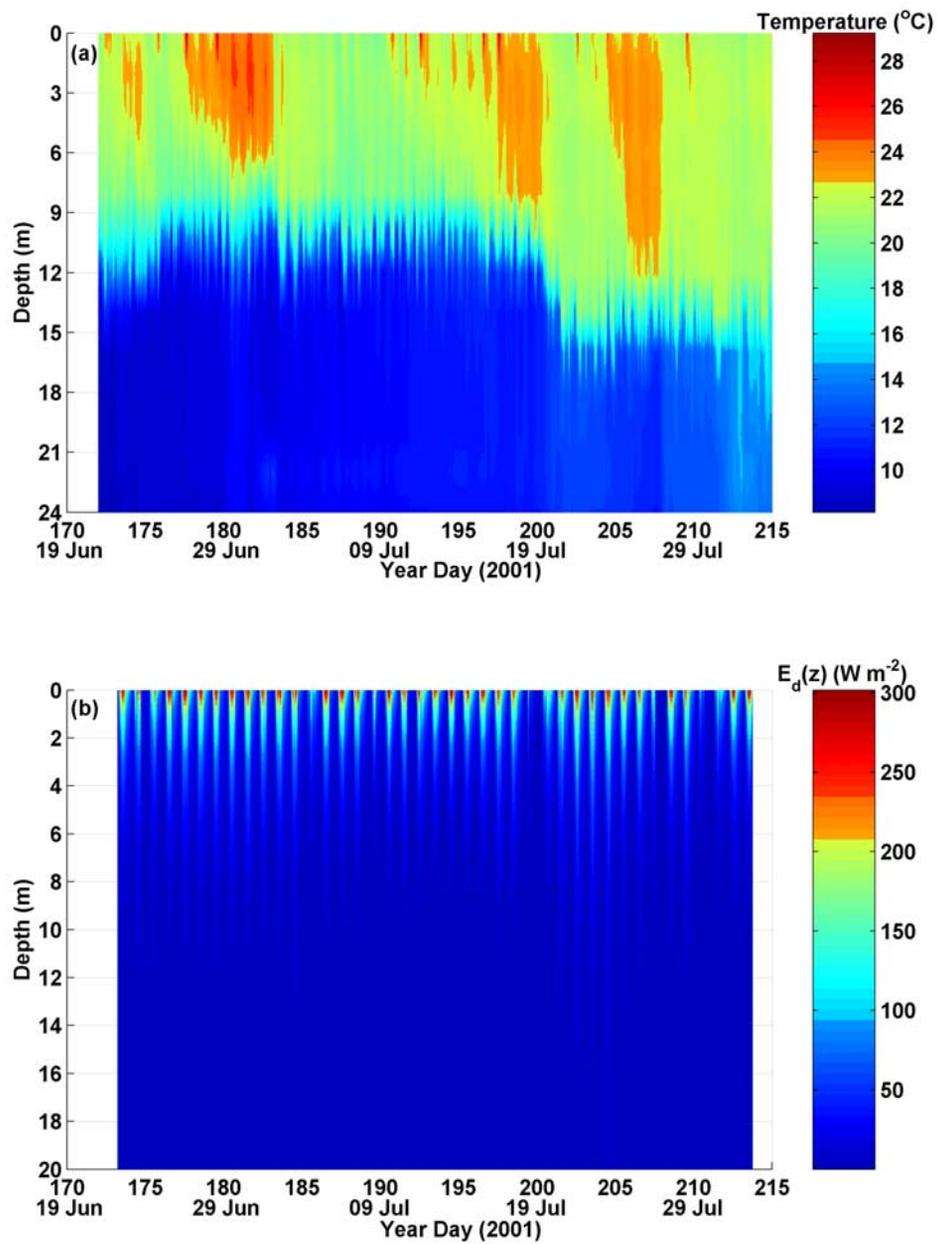
[42] These results have important implications on the development of models to quantify primary productivity and the heat budget of the coastal ocean. Models that employ simple water type classifications and parameterizations used for the open ocean are not valid in the coastal ocean as it is highly variable in terms of optically important constituents, and time and space scales of variability. This study shows that direct optical and bio-optical measurements are critical for primary production and thermodynamic models in the coastal ocean. These models can be improved with the advent of hyperspectral ocean color remote sensing and in situ technology that can sample at spatial scales on the order of 10s of m and temporal scales of <1 Hz.

References

Ackleson, S. G., W. M. Balch, and P. M. Holligan (1988), White waters of the Gulf of Maine, *Oceanography*, 1(2), 18–22.

Ackleson, S. G., W. M. Balch, and P. M. Holligan (1994), The response of water-leaving radiance to particulate calcite and pigment concentration: A model for Gulf of Maine coccolithophore blooms, *J. Geophys. Res.*, 99, 7483–7499.

Baker, K. S., and R. Frouin (1987), Relation between photosynthetically available radiation and total insolation at the ocean surface under clear skies, *Limnol. Oceanogr.*, 32, 1370–1377.

Balch, W. M., P. M. Holligan, S. G. Ackleson, and K. J. Voss (1991), Biological and optical properties of mesoscale coccolithophore blooms in the Gulf of Maine, *Limnol. Oceanogr.*, 36, 629–643.

Boss, E., W. S. Pegau, J. R. V. Zaneveld, and A. H. Barnard (2001), Spatial and temporal variability of absorption by dissolved material at a continental shelf, *J. Geophys. Res.*, 106, 9499–9507.

Chang, G. C., and T. D. Dickey (2001), Optical and physical variability on timescales from minutes to the seasonal cycle on the New England Shelf: July 1996–June 1997, *J. Geophys. Res.*, 106, 9435–9453.

Chang, G. C., T. D. Dickey, O. M. Schofield, A. D. Weidemann, E. Boss, W. S. Pegau, M. A. Moline, and S. M. Glenn (2002), Nearshore physical processes and bio-optical properties in the New York Bight, *J. Geophys. Res.*, 107(C9), 3133, doi:10.1029/2001JC001018.

Chang, G. C., T. D. Dickey, E. Boss, C. D. Mobley, and W. S. Pegau (2003), Toward closure of upwelling radiance in coastal waters, *Appl. Opt.*, 42, 1574–1582.

Dickey, T., and P. Falkowski (2002), Solar energy and its biological-physical interactions in the sea, in *The Sea*, vol. 12, edited by A. R. Robinson, J. J. McCarthy, and B. J. Rothstein, 401–440.

Dickey, T. D., and J. J. Simpson (1983), The influence of optical type on the diurnal response of the upper ocean, *Tellus*, 35, 142–151.

Dickey, T., J. Marra, D. E. Sigurdson, R. A. Weller, C. S. Kinkade, S. E. Zedler, J. D. Wiggert, and C. Langdon (1998), Seasonal variability of bio-optical and physical properties in the Arabian Sea: October 1994–October 1995, *Deep Sea Res., Part II*, 45, 2001–2025.

Doney, S. C. (1996), A synoptic atmospheric surface forcing data set and physical upper ocean model for the U.S. JGOFS Bermuda Atlantic Time-Series Study site, *J. Geophys. Res.*, 101, 25,615–25,634.

Edwards, A. M., T. Platt, and D. G. Wright (2001), Biologically induced circulation at fronts, *J. Geophys. Res.*, 106, 7081–7095.

Emery, W. J., and R. E. Thomson (1997), *Data Analysis Methods in Physical Oceanography*, Pergamon, New York.

Jiang, S., G. Chang, D. Manov, F. Spada, and T. Dickey (2001), Data Report: Hyperspectral Coastal Ocean Dynamics Experiment (HyCODE) Deployment III: 19 June–6 August 2001, *Ocean Physics Laboratory Tech. Rep. OPL-02-01*, 58 pp., Ocean Physics Lab., Univ. of Calif. at Santa Barbara, Santa Barbara, Calif.

Katsaros, K. B., L. A. McMurdie, R. J. Lind, and J. E. DeVault (1985), Albedo of a water surface, spectral variation, effects of atmospheric transmittance, sun angle, and wind speed, *J. Geophys. Res.*, 90, 7313–7321.

Kirk, J. T. O. (1988), Solar heating of water bodies as influenced by their inherent optical properties, *J. Geophys. Res.*, 93, 10,897–10,908.

Kirk, J. T. O. (1994), *Light and Photosysnthesis in Aquatic Ecosystems*, 2nd edition, Cambridge Univ. Press, New York.

Klein, P. (1980), A simulation of the effects of air-sea transfer variability on the structure of marine upper layers, *J. Phys. Oceanogr.*, 10, 1824–1841.

Lee, M. E., and M. R. Lewis (2003), Measurement of the optical volume scattering function in the upper ocean, *J. Atmos. Oceanogr. Tech.*, 20(4), 563–571.

Lewis, M. R., J. J. Cullen, and T. Platt (1983), Phytoplankton and thermal structure in the upper ocean: Consequences of nonuniformity in chlorophyll profile, *J. Geophys. Res.*, 88, 2565–2570.

Lewis, M. R., M.-E. Carr, G. C. Feldman, W. Esaias, and C. McClain (1990), Influence of penetrating solar radiation on the heat budget of the equatorial Pacific Ocean, *Nature*, 347, 543–545.

Maffione, R. A., and D. R. Dana (1997), Instruments and methods for measuring the backward-scattering coefficient of ocean waters, *Appl. Opt.*, 36, 6057–6067.

Mobley, C. D. (1994), *Light and Water: Radiative Transfer in Natural Waters*, Academic, San Diego, Calif.

Mobley, C. D., L. K. Sundman, and E. Boss (2002), Phase function effects on oceanic light fields, *Appl. Opt.*, 41, 1035–1050.

Moore, C., J. R. V. Zaneveld, and J. C. Kitchen (1992), Preliminary results from *in situ* spectral absorption meter data, *SPIE*, 1750, 330–337.

Morel, A., and D. Antoine (1994), Heating rate within the upper ocean in relation to its bio-optical state, *J. Phys. Oceanogr.*, 24, 1652–1665.

Nittrouer, C. A., and L. D. Wright (1994), Transport of particles across continental shelves, *Rev. Geophys.*, 32, 85–113.

Ohlmann, J. C., and D. A. Siegel (2000), Ocean radiant heating. Part II: Parameterizing solar radiation transmission through the upper ocean, *J. Phys. Oceanogr.*, 30, 1849–1865.

Ohlmann, J. C., D. A. Siegel, and C. D. Mobley (2000), Ocean radiant heating. Part I: Optical influences, *J. Phys. Oceanogr.*, 30, 1833–1848.

Pegau, W. S. (2002), Inherent optical properties of the Central Arctic surface waters, *J. Geophys. Res.*, 107(C10), 8035, doi:10.1029/2000JC000382.

Petzold, T. J. (1972), Volume scattering functions for selected ocean waters, *Tech. Report SIO 72–78*, Scripps Inst. Oceanogr., San Diego, 79 pgs.

Pope, R. M., and E. S. Fry (1997), Absorption spectrum (380–700 nm) of pure water. II. Integrating cavity measurements, *I. Appl. Opt.*, 36, 8710–8723.

Prieur, L., and S. Sathyendranath (1981), An optical classification of coastal and oceanic waters based on the specific spectral absorption curves of phytoplankton pigments, dissolved organic matter, and other particulate materials, *Limnol. Oceanogr.*, 26, 671–689.

Ramp, S. R., R. W. Garwood, C. O. Davis, and R. L. Snow (1991), Surface heating and patchiness in the coastal ocean off central California during a wind relaxation event, *J. Geophys. Res.*, 96, 14,947–14,957.

Siegel, D. A., J. C. Ohlmann, L. Washburn, R. R. Bidigare, C. T. Nosse, E. Fields, and Y. Zhou (1995), Solar radiation, phytoplankton pigments and the radiant heating of the equatorial Pacific warm pool, *J. Geophys. Res.*, 100, 4885–4891.

Simpson, J. J., and T. D. Dickey (1981), The relationship between downward irradiance and upper ocean structure, *J. Phys. Oceanogr.*, 11, 309–323.

Sosik, H. M., R. E. Green, W. S. Pegau, and C. S. Roesler (2001), Temporal and vertical variability in optical properties of New England shelf waters during late summer and spring, *J. Geophys. Res.*, 106, 9455–9472.

Thompson, R. O. R. Y. (1979), Coherence significance levels, *J. Atmos Sci.*, 36, 2020–2021.

Woods, J. D., W. Barkmann, and A. Horch (1984), Solar heating of the oceans-diurnal, seasonal, and meridional variation, *Q. J. R. Meteorol. Soc.*, 110, 633–656.

Zaneveld, J. R. V., J. C. Kitchen, and H. Pak (1981), The influence of optical water type on the heating rate of a constant depth mixed layer, *J. Geophys. Res.*, 86, 6426–6428.

_____

G. C. Chang and T. D. Dickey, Ocean Physics Laboratory, University of California, Santa Barbara, Goleta, CA 93117, USA. (grace.chang@opl.ucsb.edu)

Figure 2. Time series contour plots of hourly averaged (a) temperature with depth and (b) spectrally integrated ($\lambda = 400-800$ nm) downwelling irradiance with depth, $E_d(z)$, derived from HyCODE mooring measurements and equations (11) and (12).